Acta Oceanol. Sin., 2021, Vol. 40, No. 12, P. 148–160
https://doi.org/10.1007/s13131-021-1867-2
http://www.aosocean.com
E-mail: ocean2@hyxb.org.cn

An improved optical flow method to estimate Arctic sea ice velocity (winter 2014–2016)

Haili Li[1, 2, 3], Changqing Ke[1, 2, 3*], Qinghui Zhu[1, 2, 3], Xiaoyi Shen[1, 2, 3], Mengmeng Li[1, 2, 3]

[1] Jiangsu Provincial Key Laboratory of Geographic Information Science and Technology/Key Laboratory for Land Satellite Remote Sensing Applications of Ministry of Natural Resources, School of Geography and Ocean Science, Nanjing University, Nanjing 210023, China

[2] Collaborative Innovation Center of Novel Software Technology and Industrialization, Nanjing 210023, China

[3] Collaborative Innovation Center of South China Sea Studies, Nanjing 210023, China

Received 18 January 2021; accepted 12 June 2021

Abstract

Sea ice velocity impacts the distribution of sea ice, and the flux of exported sea ice through the Fram Strait increases with increasing ice velocity. Therefore, improving the accuracy of estimates of the sea ice velocity is important. We introduce a pyramid algorithm into the Horn-Schunck optical flow (HS-OF) method (to develop the PHS-OF method). Before calculating the sea ice velocity, we generate multilayer pyramid images from an original brightness temperature image. Then, the sea ice velocity of the pyramid layer is calculated, and the ice velocity in the original image is calculated by layer iteration. Winter Arctic sea ice velocities from 2014 to 2016 are obtained and used to discuss the accuracy of the HS-OF method and PHS-OF (specifically the 2-layer PHS-OF (2LPHS-OF) and 4-layer PHS-OF (4LPHS-OF)) methods. The results prove that the PHS-OF method indeed improves the accuracy of sea ice velocity estimates, and the 2LPHS-OF scheme is more appropriate for estimating ice velocity. The error is smaller for the 2LPHS-OF velocity estimates than values from the Ocean and Sea Ice Satellite Application Facility and the Copernicus Marine Environment Monitoring Service, and estimates of changes in velocity by the 2LPHS-OF method are consistent with those from the National Snow and Ice Data Center. Sea ice undergoes two main motion patterns, i.e., transpolar drift and the Beaufort Gyre. In addition, cyclonic and anticyclonic ice drift occurred during winter 2016. Variations in sea ice velocity are related to the open water area, sea ice retreat time and length of the open water season.

Key words: winter sea ice velocity, pyramid Horn-Schunck optical flow (PHS-OF) method, transpolar drift, Beaufort Gyre, open water, Arctic

Citation: Li Haili, Ke Changqing, Zhu Qinghui, Shen Xiaoyi, Li Mengmeng. 2021. An improved optical flow method to estimate Arctic sea ice velocity (winter 2014–2016). Acta Oceanologica Sinica, 40(12): 148–160, doi: 10.1007/s13131-021-1867-2

1 Introduction

It is widely known that the sea ice extent has decreased rapidly (Parkinson et al., 1999; Cavalieri et al., 2003; Ke et al., 2013; Comiso et al., 2017), and the open water area has increased significantly (Arrigo and Van Dijken, 2011; Li and Ke, 2017). In addition to thermodynamic factors such as albedo that impact sea ice changes (Zhang et al., 2000; Massom and Stammerjohn, 2010), sea ice drift also contributes to sea ice changes from a dynamic perspective (Allison, 1989). High sea ice velocity causes greater loss of sea ice that flows out of the Arctic Ocean (Min et al., 2019). In addition, sea ice drift affects the safety of ship navigation (Mäkynen et al., 2020). Therefore, many scholars are devoted to studying sea ice drift (Zuo et al., 2016; Qiu et al., 2019; Zhao and Liu, 2007). A negative trend in multiyear sea ice coverage over 90% of the Arctic Ocean and a positive trend in sea ice speed were reported (Kwok et al., 2013). In addition to Arctic sea ice speed, Antarctic sea ice speed generally increased from 1979 to 2014, and the strength of wind had a great effect on the increase in the sea ice speed (Liu et al., 2019).

Many studies on sea ice velocity estimation have been implemented to better and more accurately understand the variations in sea ice (Meier and Dai, 2006; Girard-Ardhuin and Ezraty, 2012; Komarov and Barber, 2014). At present, the most used method is the maximum cross-correlation (MCC) approach, which is a pattern matching method. Ninnis et al. (1986) first introduced the MCC method for sea ice estimation with Advanced Very High Resolution Radiometer (AVHRR) data, and it was proven to be effective in reproducing the sea ice drift field. Since then, many scholars have used this method to estimate sea ice drift (Agnew et al., 1997; Emery et al., 1997; Lavergne et al., 2010). Kwok et al. (1998) first confirmed that 37-GHz Special Sensor Microwave/Imager (SSM/I) data can be used to retrieve sea ice drift. Lehtiranta et al. (2015) first compared sea ice velocity derived from different bands synthetic aperture radar (SAR) images (L-bands and C-bands) with the MCC method. To investigate shorter displacements for low-resolution sensors, Lavergne et al. (2010) introduced the continuous MCC (CMCC) method, which depends on a continuous optimization step. The great majority of well-known sea ice motion estimates are obtained by the MCC method, such as those from the National Snow and Ice Data Center

Foundation item: The National Key Research and Development Program of China under contract Nos 2018YFC1407200 and 2018YFC1407203; the National Natural Science Foundation of China under contract No. 41976212.
*Corresponding author, E-mail: kecq@nju.edu.cn

(NSIDC) and the Ocean and Sea Ice Satellite Application Facility (OSI SAF).

There are some other approaches for estimating sea ice velocity. Wavelet-based methods and principal component analysis (PCA)-based methods have been developed to reproduce sea ice velocity. Liu and Cavalieri (1998) utilized wavelet analysis to obtain daily Arctic and Antarctic sea ice motion information from Defense Meteorological Satellite Program (DMSP) SSM/I 85-GHz radiance data. Liu et al. (1999) further used the National Aeronautics and Space Administration (NASA) Scatterometer (NSCAT) backscatter and DMSP SSM/I radiance data to successfully estimate daily sea ice drift in the Arctic by wavelet analysis. Borcea et al. (2012) adopted PCA for SAR imagery, solving the problems associated with the detection of moving targets in complex scenes. The optical flow (OF) method, which was first introduced for Antarctic sea ice motion estimation by Gutiérrez and Long (2003), was proven to effectively estimate sea ice velocity. The OF method relies on the brightness constancy assumption (Fleet and Weiss, 2006), and the relative displacement of each pixel is calculated. Therefore, a dense velocity field can be obtained. Based on Geostationary Ocean Color Imager (GOCI) data, Wu et al. (2014) used the OF method to obtain the ice velocity in the Bohai Sea and proved that it was in good agreement with the selected reference data. Based on the OF algorithm, Petrou and Tian (2017) used Moderate Resolution Spectroradiometer (MODIS) data to produce a high-resolution sea ice drift field and found that the OF method provided more accurate results than the MCC method. The feature tracking algorithm is a useful method that has been rapidly developed in recent years. With Sentinel-1 SAR imagery, Muckenhuber et al. (2016) adopted an open-source feature tracking algorithm (oriented features from accelerated segment test and rotated binary robust independent elementary features (ORB)) to estimate sea ice drift and found that it was computationally efficient. Muckenhuber and Sandven (2018) found that displacement gradients can be resolved by using the ORB algorithm at a very high resolution. Some researchers focus on improving sea ice drift estimation algorithms. Based on the MCC method, Wang et al. (2017) employed the Laplacian of a Gaussian filter to calculate the sea ice velocity with 37-GHz brightness temperature (BT) data from the Haiyang-2 (HY-2) satellite. They found that this approach is useful for obtaining a dense velocity field and improving the accuracy. Berg and Eriksson (2014) combined pattern matching with feature tracking to measure sea ice drift. Petrou et al. (2018) used the OF method combined with a super-resolution approach to obtain more accurate motion vectors.

Among these methods, the optical flow and feature tracking algorithms are newer than other methods. It has been proven that the OF method is more efficient than the MCC method for sea ice drift estimation (Petrou and Tian, 2017). It has a higher accuracy and shorter calculation time and can produce a dense sea ice drift field. Feature tracking algorithms are more appropriate for high-resolution images such as SAR. The OF method is based on computer vision and can be used with different data. Recently, the OF method has become a popular approach for vehicle speed measurement (Lan et al., 2014; Lim et al., 2019; Ke et al., 2019) based on videos. Petrou et al. (2018) proved that the OF method is suitable for microwave radiometer images, optical images and SAR. Although the OF method has many advantages in calculating the sea ice velocity, it greatly underestimates the velocity when sea ice moves fast. To obtain an accurate value for assessing sea ice motion to analyze sea ice change, a better sea ice drift estimation method based on the OF method needs to be developed. Based on the brightness temperature data from the NSIDC, we propose an improved Horn-Schunck optical flow (HS-OF) method developed by introducing the pyramid algorithm into the HS-OF method and calculate the daily winter sea ice velocity from 2014 to 2016. Then, we further compare the sea ice velocity from this study with three well-known sea ice drift estimates from the NSIDC, OSI SAF and Copernicus Marine Environment Monitoring Service (CMEMS) and analyze the variations in the sea ice velocity during winter 2016.

2 Study area, data and methods

2.1 *Study area*

According to the method of Cavalieri and Parkinson (2012), the Arctic is divided into nine subregions (Fig. 1): the Arctic Ocean (the core of the Arctic), which includes the Beaufort Sea (BFS), Chukchi Sea (CS), East Siberian Sea (ESS) and Laptev Sea (LS) (Peng and Meier, 2018); the Canadian Archipelago, which is located north of Canada; the Bering Sea; the seas of Okhotsk and Japan; the Kara and Barents seas (with Novaya Zemlya as the boundary between the Kara and Barents seas); the Greenland Sea; the Hudson Bay; the Baffin Bay/Labrador Sea; and the Gulf of St. Lawrence. The Bering Sea and the Arctic Ocean are connected by the Bering Strait, and the Greenland Sea is connected with the Arctic Ocean by the Fram Strait (FS). The study area includes not only the polar regions within the Arctic Circle but also some mid-latitude regions that are covered by sea ice (Deng, 2014; Li and Ke, 2017).

2.2 *Data and preprocessing*

2.2.1 *Brightness temperature and sea ice concentration*

Daily brightness temperature and sea ice concentration (SIC) data are provided by the NSIDC. Brightness temperatures can be measured with SSM/I and Special Sensor Microwave Imager/Sounder (SSMIS) instruments. The DMSP SSM/I-SSMIS daily polar gridded brightness temperatures, Version 5 is selected, including data at 19 GHz, 22 GHz, 37 GHz and 85/91 GHz. Except for 22 GHz data, the others include horizontal polarization and vertical polarization data. High-frequency data are effective for sea ice velocity estimation. Therefore, we select the 37 GHz data (spatial resolution of 25 km×25 km) and 91 GHz data (spatial resolution of 12.5 km×12.5 km) from January to March (i.e., winter), 2014–2016.

The selected SIC data have a spatial resolution of 25 km×25 km, i.e., Nimbus-7 scanning multichannel microwave radiometer (SMMR) DMSP SSM/I-SSMIS passive microwave data, Version 1, and near-real-time DMSP SSMIS Daily polar gridded sea ice concentration data. The data covering the period from January to March 2014–2016 are selected to create sea ice masks for extracting the brightness temperatures for areas covered with sea ice.

2.2.2 *Buoy data and sea ice motion*

The International Arctic Buoy Programme (IABP) was established in 1991. It provides meridional and zonal sea ice velocities, which are obtained by interpolating buoy data from 1979 to 2016 in DAT or TXT format. We select the buoy-derived sea ice velocity from January to March 2014–2016 to evaluate the accuracy of the estimated ice velocity calculated by the improved optical flow method.

We select and compare three daily sea ice motion estimates from January to March 2014–2016. Table 1 shows the information for the sea ice drift data we selected. The first set of data is

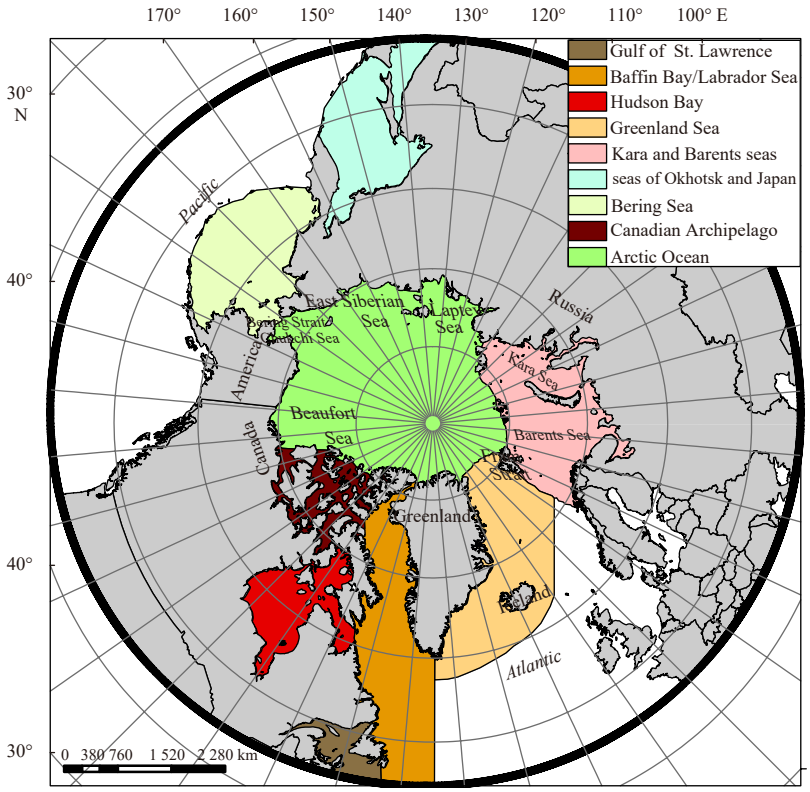

Fig. 1. Map of the locations of the nine subregions of the Arctic.

Table 1. Statistics for three sea ice drift datasets

Data provider	NSIDC	OSI SAF	CMEMS
Sensor	AMSR-E, AVHRR, drifting buoys, SMMR, SSM/I, SSMIS	AMSR-2, SSMIS, ASCAT	AMSR-E, AMSR-2, SSM/I, SSMIS, QuickSCAT, ASCAT
Spatial resolution	25 km×25 km	62.5 km×62.5 km	12.5 km×12.5 km
Method	MCC	CMCC	CMCC, model

provided by the NSIDC, and its spatial resolution is 25 km×25 km. It merges the sea ice velocities of the Advanced Microwave Scanning Radiometer-E (AMSR-E), AVHRR, drifting buoys, SMMR, SSM/I, and SSMIS based on the MCC method. The second set of data is provided by the OSI SAF and calculated by adopting the CMCC approach. The OSI SAF offers low-resolution (LR) sea ice drift and medium-resolution (MR) sea ice drift data. Because the sea ice drift calculated in this study relies on SSM/I and SSMIS sensors, we select the LR sea ice drift data from the OSI SAF with a spatial resolution of 62.5 km×62.5 km. The last set of data is from the CMEMS and has a spatial resolution of 12.5 km× 12.5 km. It is calculated by assimilating the satellite-derived sea ice drift, which is provided by the Center for Satellite Exploitation and Research (CERSAT) and OSI SAF, into the TOPAZ4 system (Sakov et al., 2012; CMEMS, 2020).

2.2.3 *Data preprocessing*

The initial SIC data are gray values between 0 and 255, and we presume that a value of 251 indicates 100% sea ice (Deng, 2014), and values of 252, 253, 254 and 255 indicate unused data, coastlines data, land data and missing data, respectively. We divide each gray values by 251 to obtain a value in the 0%–100% range. The BT dataset is a BIN file, so we convert the BIN file to a TIF file and define the polar azimuth projection. After preparing the SIC and BT data, we extract the sea ice region where SIC is greater than or equal to 15% to create a sea ice mask dataset. Then, we clip the BT data with a sea ice mask to extract the brightness temperature of the sea ice. Finally, a wavelet filter is used to smooth the image.

To match other datasets, OSI SAF and CMEMS data are resampled to a 25 km×25 km grid. The x-axis of the buoy product coincides with the Greenwich meridian, and the y-axis coincides with the 90°E meridian. The x-axes of three sea ice motion datasets (OSI SAF, CMEMS and this study) coincide with the 45°E meridian, the y-axes coincide with the 135°E meridian; the x-axis of the NSIDC product coincides with the 90°E meridian, and the y-axis coincides with the 180°E meridian. When accuracy verification is performed, the x- and y-axes of the speed datasets from the buoy, OSI SAF, CMEMS and this study are converted to the same direction as those from the motion dataset from the NSIDC.

2.3 *Methods*

2.3.1 *The Horn-Schunck optical flow method*

Compared with the MCC method, the optical flow method has the advantages of obtaining a dense velocity field and capturing more velocity details. The brightness constancy assumption is the basic assumption of all optical flow methods. It states that the brightness of a pixel remains constant as it moves (Petrou and Tian, 2017). The HS-OF method (Horn and Schunck, 1981), a typical representative of the gradient-based method, assumes that the velocity vector field in a given neighborhood changes slowly. According to these two assumptions, iterative equations

for calculating sea ice velocity are acquired:

$$u^{(k+1)} = u_{\mathrm{Avg}}{}^{(k)} - I_x(I_x u_{\mathrm{Avg}}{}^{(k)} + I_y v_{\mathrm{Avg}}{}^{(k)} + I_t)/(\lambda^2 + I_x^2 + I_y^2), \quad (1)$$

$$v^{(k+1)} = v_{\mathrm{Avg}}{}^{(k)} - I_y(I_x u_{\mathrm{Avg}}{}^{(k)} + I_y v_{\mathrm{Avg}}{}^{(k)} + I_t)/\left(\lambda^2 + I_x^2 + I_y^2\right), \quad (2)$$

where u represents the speed in the horizontal direction (x), and v represents the speed in the vertical direction (y); n is the number of iterations (k=1, 2, 3,⋯, $k \leqslant n$), which can be set to 100 when few changes occur after 64 iterations (Horn and Schunck, 1981); I_x and I_y are partial derivatives of the image function in the x-axis and y-axis, respectively; I_t is the partial derivative of the image function in the time; λ reflects the credibility of the image smoothing with a default value of 1; and u_{Avg} and v_{Avg} represent the average values in the u domain and v domain, respectively.

u_{Avg} (v_{Avg}) is obtained from a convolution of u (v) with the average value template, which is [1/12 1/6 1/12; 1/6 0 1/6; 1/12 1/6 1/12]. The center position of the template is aligned with the pixel to be solved in the image, and nine pixels, including the center pixel, are multiplied with values of the template at the corresponding position and then summed to calculate the central pixel value, i.e., the average value of the pixel. Finally, the average value of every pixel in the image can be obtained (u_{Avg} and v_{Avg}).

2.3.2 *Pyramid optical flow method*

The HS-OF method is used under the assumption that the sea ice drift is small, but this assumption is difficult to satisfy in reality. To use this method when the motion of sea ice is large, an improved optical flow method is developed. The concept of pyramids (Choudhary et al., 2012) is introduced into the HS-OF method to create a method we call the PHS-OF method. We construct a multilayer pyramid image by downsampling, which means, unlike in the HS-OF method, every other row and every other column are sampled. For the top pyramid image (i.e., the n–1 layer), which has the lowest resolution and the smallest size, the HS-OF algorithm is used to calculate the results, which are carried into the next layer, and the sea ice velocity of the bottom layer (0 layer: original image) is obtained by iterative calculation. Because the pyramid image at the top layer has the smallest size, the sea ice motion distance in the two images is relatively small, which makes it easier to meet the small motion constraints of the HS-OF method. In conclusion, the PHS-OF method can convert large motions of sea ice into small motions to estimate sea ice velocity more accurately than the HS-OF method.

The detailed steps of the PHS-OF method are developed in this study. First, we construct a Gaussian pyramid image that uses a Gaussian low-pass filter in the image construction process (Fig. 2a). The original input image is processed by Gaussian filtering, and downsampling is performed to obtain the first layer image. Then, the first layer image is processed by Gaussian filtering and downsampling to obtain the second layer image and so on to obtain the n–1 layer image. The area of the image in the next layer is four times that of the image on the previous layer. The smallest image is at the top layer, and the original image is at

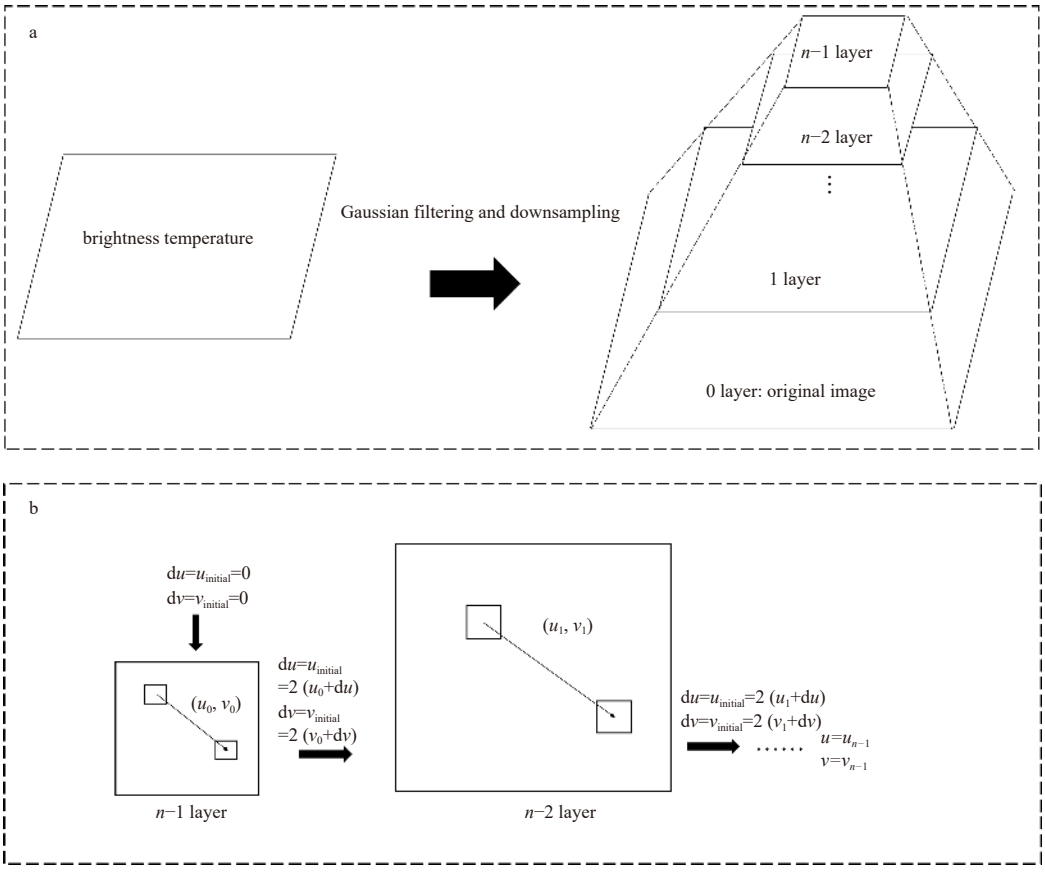

Fig. 2. n-layer pyramid image construction process (a), and flow chart of the n-layer pyramid HS-OF method (b). The bottom layer (0 layer) represents the original image, and the top layer represents the smallest image. The thin arrows in b indicate the direction of sea ice drift.

the bottom. Second, we set the initial value of the velocity calculation to 0, and then the initial sea ice motion values are assigned to du and dv. Next, we use the HS-OF method to calculate the optical flow vector (u_0, v_0) of the top image (the n–1 layer). Third, we add the vector of this layer to the initial sea ice motion vector (du, dv) and then multiply by 2 to obtain the initial value of the next layer (2(u_0+du, v_0+dv)) (Fig. 2b). Thus, the sea ice drift vector of the lowest layer (the original image: u_{n-1}, v_{n-1}) can be obtained.

2.3.3 *Merging scheme*

We adopt two merging schemes to obtain the final merged data set. The first scheme is used to merge horizontal (H) polarization data and vertical (V) polarization data. First, we calculate the sum of the absolute velocity (S), and then the ratio of the horizontal polarization absolute velocity to S, which is the weight of the H-polarization velocity. Similarly, the weight of the V-polarization velocity is obtained. Finally, we calculate the polarization-merged velocity.

The second merging scheme is used with different frequency data (i.e., 37 GHz and 91 GHz). Before merging, the velocity from the 91-GHz brightness temperature is resampled to a 25 km× 25 km grid. The velocity obtained from high-frequency brightness temperature data is more accurate than that from low-frequency brightness temperature data (NSIDC, 2019). Thus, the ice velocity from 91-GHz data should have a higher weight in the merging process. Then, we determine the weights by experimentation (adopting different weights) and obtain the optimal weights of 0.75 for 91 GHz and 0.25 for 37 GHz. After the merging process, we finally obtain the daily sea ice velocity with a spatial resolution of 25 km ×25 km.

3 Validation of Arctic sea ice velocity

3.1 *Accuracy evaluation according to buoy velocities*

Buoy velocities at the number buoy 1 (nb1) (74°N, 160°E), nb2 (74°N, 180°E), nb3 (74°N, 140°W), nb4 (78°N, 140°E), nb5 (78°N, 120°W), nb6 (82°N, 160°W), and nb7 (82°N, 80°E) positions, which are seven buoy points located in or near seven subregions of the Arctic, are chosen (Fig. 3). This ensures that the selected position is representative.

To evaluate the reliability of our results, four statistical parameters are used. P is the correlation between the satellite-derived ice velocity and the buoy velocity, which is defined by a method similar to that of Kwok et al. (1998):

$$P = \frac{\sum u_{\mathrm{pro}} \cdot u_{\mathrm{buoy}}}{\sum \left|u_{\mathrm{pro}}\right| \left|u_{\mathrm{buoy}}\right|}, \tag{3}$$

where u_{pro} is the satellite ice motion and u_{buoy} is the buoy velocity.

In addition to P, the root mean square error (RMSE), the mean error (ME), and the mean absolute error (MAE) are calculated by a method similar to that of Zhu et al. (2014) and Rossel and Webster (2012).

We use two common layering schemes (the 2-layer PHS-OF (2LPHS-OF) and 4-layer PHS-OF (4LPHS-OF)) as well as the HS-OF method to obtain three datasets of sea ice velocity during the winters of 2014–2016. For convenience, we use HS-OF velocity, 2LPHS-OF velocity and 4LPHS-OF velocity to represent sea ice velocity obtained by these three methods. For most positions, the errors in the v-velocity obtained by the HS-OF method are better than those in the u-velocity, but the correlation between the v-ve-

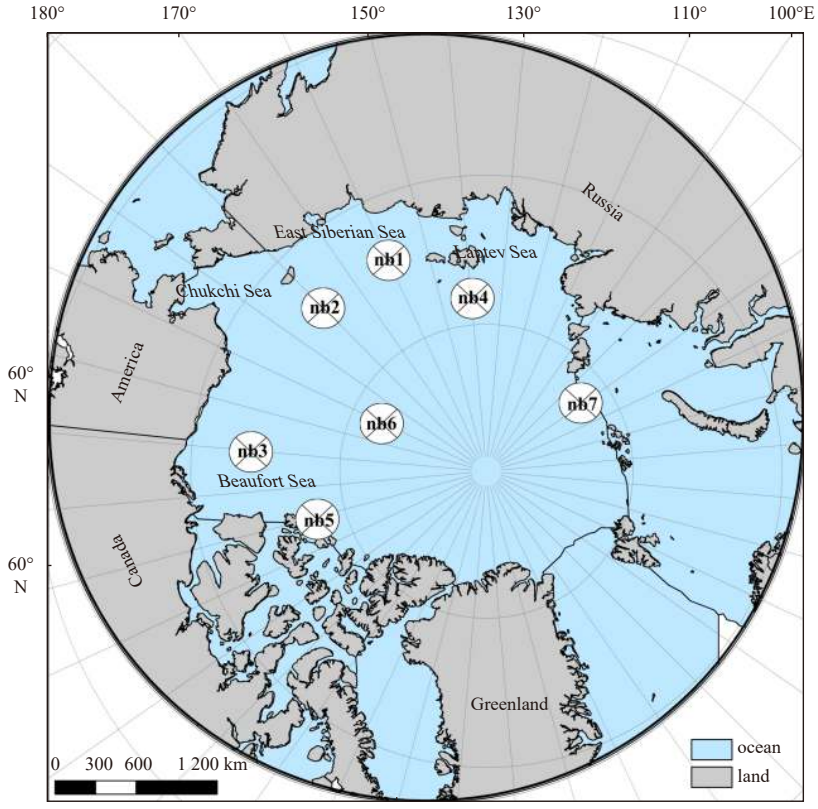

Fig. 3. Spatial distribution of the region where velocity data for buoys in the Arctic Ocean are obtained. The buoys are numbered as nb$x$ with x being 1 to 7.

locity and buoy velocity is lower than that between the *u*-velocity and buoy velocity (Table 2). Buoy velocities at the nb5 and nb7 positions correlate weakly with the HS-OF velocity (less than 0.40). Relative to the buoy velocity, HS-OF velocity is overestimated at the nb6 and nb7 positions, which are located at higher latitudes (Table 2). The results indicate that the HS-OF method can be used to estimate the sea ice velocity with a low error, especially in the LS (nb4), ESS (nb1), CS (nb2) and BFS (nb3) regions, but the correlations need to be further improved.

After we introduce the pyramid, the value of *P* is promoted in both the *u*- and *v*-directions, and the ME is reduced at almost all positions, i.e., at the nb1, nb2, nb3, nb5 and nb6 positions (Table 2). The velocity accuracies of the nb4 positions are greatly improved in the *v*-direction, but the accuracy is slightly reduced in the *u*-direction. The accuracies of velocity at the nb2, nb3, nb5 and nb7 positions are obviously greatly improved in the *u*-direction, but the accuracy is reduced to some degree in the *v*-direction. The velocity accuracies at the nb1 position are improved in both the *u*- and *v*-directions (Table 2). For the nb1 position, the 2LPHS-OF velocity has a smaller RMSE and MAE and a higher *P* than the 4LPHS-OF velocity in the *u*-direction, but it has a higher RMSE and MAE and a smaller P than the 4LPHS-OF velocity in the *v*-direction. For the nb5 position, the error of the 2LPHS-OF velocity is higher than that of the 4LPHS-OF velocity in the *u*-direction, while the 2LPHS-OF velocity is more accurate than the 4LPHS-OF velocity in the *v*-direction. For other positions, almost all accuracy indices of the 2LPHS-OF velocity are better than those of the 4LPHS-OF velocity. In conclusion, the use of the 2-

Table 2. Accuracy evaluation of the HS-OF, 2LPHS-OF and 4LPHS-OF methods for the buoy velocity positions (in the *u*-direction and *v*-direction) through RMSE, ME, MAE, and *P* from 2014 to 2016 (winter)

	u_{nb1}			v_{nb1}		
	HS-OF	2LPHS-OF	4LPHS-OF	HS-OF	2LPHS-OF	4LPHS-OF
RMSE/(cm·s^{-1})	4.83	4.79	4.88	4.20	3.99	3.96
ME/(cm·s^{-1})	–1.12	–0.79	–0.76	1.60	1.37	1.26
MAE/(cm·s^{-1})	3.63	3.63	3.72	3.10	2.97	2.91
P	0.44	0.62	0.58	0.58	0.70	0.71
	u_{nb2}			v_{nb2}		
	HS-OF	2LPHS-OF	4LPHS-OF	HS-OF	2LPHS-OF	4LPHS-OF
RMSE/(cm·s^{-1})	5.57	5.11	5.18	4.46	4.65	4.71
ME/(cm·s^{-1})	–1.95	–1.19	–1.17	0.74	0.47	0.35
MAE/(cm·s^{-1})	4.40	3.98	4.00	3.35	3.46	3.43
P	0.79	0.84	0.83	0.52	0.66	0.68
	u_{nb3}			v_{nb3}		
	HS-OF	2LPHS-OF	4LPHS-OF	HS-OF	2LPHS-OF	4LPHS-OF
RMSE/(cm·s^{-1})	5.06	4.23	4.28	3.84	4.67	5.34
ME/(cm·s^{-1})	–0.49	–0.29	-0.31	–1.78	–1.04	–0.99
MAE/(cm·s^{-1})	4.01	3.31	3.33	3.04	3.50	3.91
P	0.89	0.93	0.92	0.67	0.73	0.69
	u_{nb4}			v_{nb4}		
	HS-OF	2LPHS-OF	4LPHS-OF	HS-OF	2LPHS-OF	4LPHS-OF
RMSE/(cm·s^{-1})	3.86	4.08	4.27	4.90	4.53	5.14
ME/(cm·s^{-1})	–0.29	–0.62	–0.59	2.24	1.92	2.03
MAE/(cm·s^{-1})	3.06	3.20	3.32	3.80	3.47	3.84
P	0.64	0.69	0.72	0.64	0.76	0.62
	u_{nb5}			v_{nb5}		
	HS-OF	2LPHS-OF	4LPHS-OF	HS-OF	2LPHS-OF	4LPHS-OF
RMSE/(cm·s^{-1})	4.48	4.40	4.37	3.39	3.39	3.48
ME/(cm·s^{-1})	1.57	1.47	1.44	–1.48	–1.36	–1.33
MAE/(cm·s^{-1})	3.37	3.30	3.27	2.53	2.58	2.62
P	0.34	0.48	0.50	0.30	0.42	0.39
	u_{nb6}			v_{nb6}		
	HS-OF	2LPHS-OF	4LPHS-OF	HS-OF	2LPHS-OF	4LPHS-OF
RMSE/(cm·s^{-1})	4.92	5.25	8.12	4.20	4.67	6.80
ME/(cm·s^{-1})	1.41	1.14	1.16	0.61	0.44	0.76
MAE/(cm·s^{-1})	3.69	3.92	5.80	3.34	3.59	4.49
P	0.35	0.44	0.36	0.43	0.52	0.61
	u_{nb7}			v_{nb7}		
	HS-OF	2LPHS-OF	4LPHS-OF	HS-OF	2LPHS-OF	4LPHS-OF
RMSE/(cm·s^{-1})	4.72	4.70	5.30	5.92	5.99	6.17
ME/(cm·s^{-1})	2.86	2.37	2.37	2.30	2.42	2.54
MAE/(cm·s^{-1})	4.13	4.04	4.45	5.36	5.42	5.55
P	0.38	0.54	0.52	0.25	0.37	0.33

layer pyramid greatly enhances the value of P for velocity and makes the results tend toward the real sea ice drift velocity. With four layers, the error is increased, indicating that using more layers does not improve the accuracy.

We also calculate the computing time for obtaining the sea ice velocity from two images. The more layers in a pyramid, the longer it takes to run the computation. The HS-OF, 2LPHS-OF and 4LPHS-OF methods take 1.56 s, 1.91 s and 2.06 s, respectively.

We obtain the average accuracy at the above positions (Table 3). The errors of the 4LPHS-OF velocity are much higher than those of the HS-OF and 2LPHS-OF velocities. The error in the v-velocity is slightly less than that in the u-velocity, but the correlation for the v-velocity is less than that for the u-velocity. The accuracy of the 2LPHS-OF velocity is better than that of the HS-OF velocity, which greatly reduces the RMSE (it decreases 3%) and MAE (it decreases 4%) and improves the P (14%) in the u-direction. It also reduces the ME (1%) and improves the P (21%) in the v-direction. The HS-OF u-velocity at all positions except the nb4 position has a higher ME than the 2LPHS-OF u-velocity (Table 2). However, after averaging the ME of all seven points, the biases cancel each other out, resulting in a lower ME (Table 3). In total, although the RMSE (–3%) and MAE (–2%) in the 2LPHS-OF velocity in the v-direction increase, the correlation between the buoy velocity and satellite-derived velocity is greatly improved, and there are more accurate velocities in the u-direction.

Figure 4 shows scatterplots of the HS-OF, 2LPHS-OF, and 4LPHS-OF velocities versus the buoy average velocity. The x-axis is the buoy velocity, and the y-axis is the satellite-derived sea ice velocity. There is a positive correlation between the HS-OF velocity and the buoy velocity, but a certain gap exists between the fitting line and the baseline (one-by-one fitting line) (Figs 4a and d). After pyramid processing, the scattered points are more concentrated near the baseline, and the angle between the fitting line and the baseline decreases (Figs 4b and e). Some points of the 4LPHS-OF velocity are farther away from the baseline, and the fitting line is closer to the baseline than the fitting line of the 2LPHS-OF velocity (Figs 4c and f).

Among the above positions, we select four positions that are dispersed geographically to analyze variations in sea ice velocities from 2014 to 2016 (Fig. 5). Generally, the retrieved velocities are lower than the buoy velocity, and the optical flow method underestimates the sea ice velocity. Although the PHS-OF velocity is still lower than the buoy velocity, the difference between the PHS-OF velocity and the buoy velocities decreases (Fig. 5). Compared with that in 2014, the trend in the PHS-OF velocity in 2015 and 2016 is more consistent with the buoy velocity. With the increase in pyramid layers, the retrieved results are increasingly close to the buoy velocity. However, from late January to February, an obvious overestimation of the drift speed occurs at the nb2 position in 2014 and the nb4 position in 2016 when four pyramid layers are adopted (Figs 5a–d). When the HS-OF method overestimates ice velocity, the use of two pyramid layers in-

Table 3. Overall accuracy evaluation of the HS-OF, 2LPHS-OF and 4LPHS-OF methods in the u-direction and v-direction through the RMSE, ME, MAE, and P based on buoy velocity from 2014 to 2016 (winter, a total of 1 829 matchup data)

	u			v		
	HS-OF	2LPHS-OF	4LPHS-OF	HS-OF	2LPHS-OF	4LPHS-OF
RMSE/(cm·s^{-1})	4.89	**4.76**	5.45	4.56	**4.70**	5.29
ME/(cm·s^{-1})	0.19	**0.22**	0.23	0.54	**0.54**	0.59
MAE/(cm·s^{-1})	3.74	**3.61**	3.97	3.44	**3.48**	3.76
P	0.61	**0.70**	0.65	0.50	**0.60**	0.59

Note: The bolded values are the 2LPHS-OF volocity.

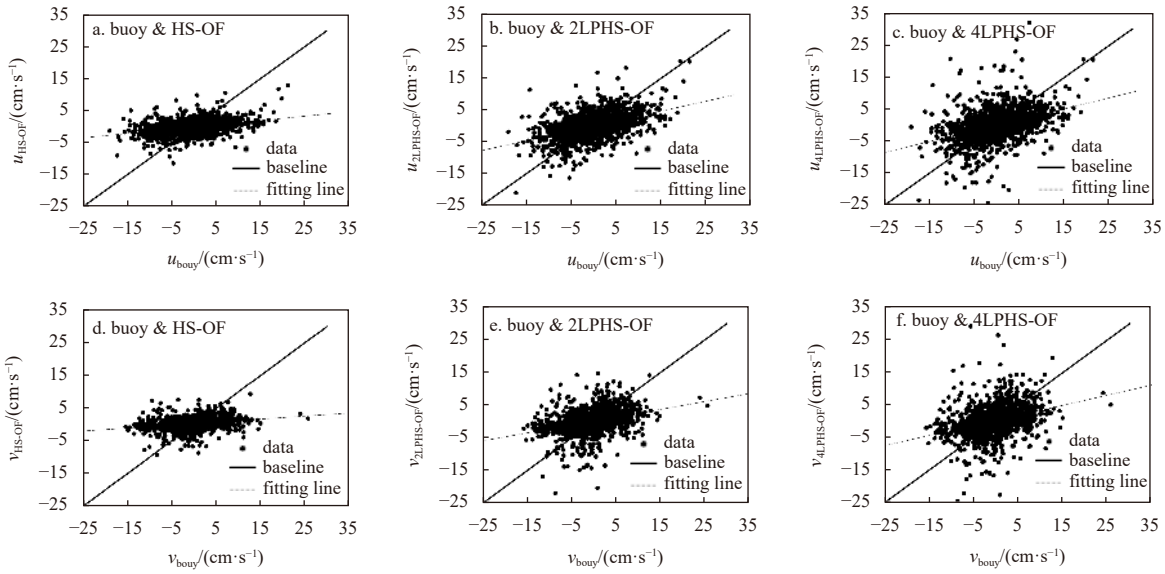

Fig. 4. Scatterplots of the data obtained by the HS-OF, 2LPHS-OF and 4LPHS-OF methods versus the buoy data in the u (x) and v (y) directions. a, b and c. HS-OF velocity, 2LPHS-OF velocity and 4LPHS-OF velocity in the u-direction; and d, e and f. HS-OF velocity, 2LPHS-OF velocity and 4LPHS-OF velocity in the v-direction.

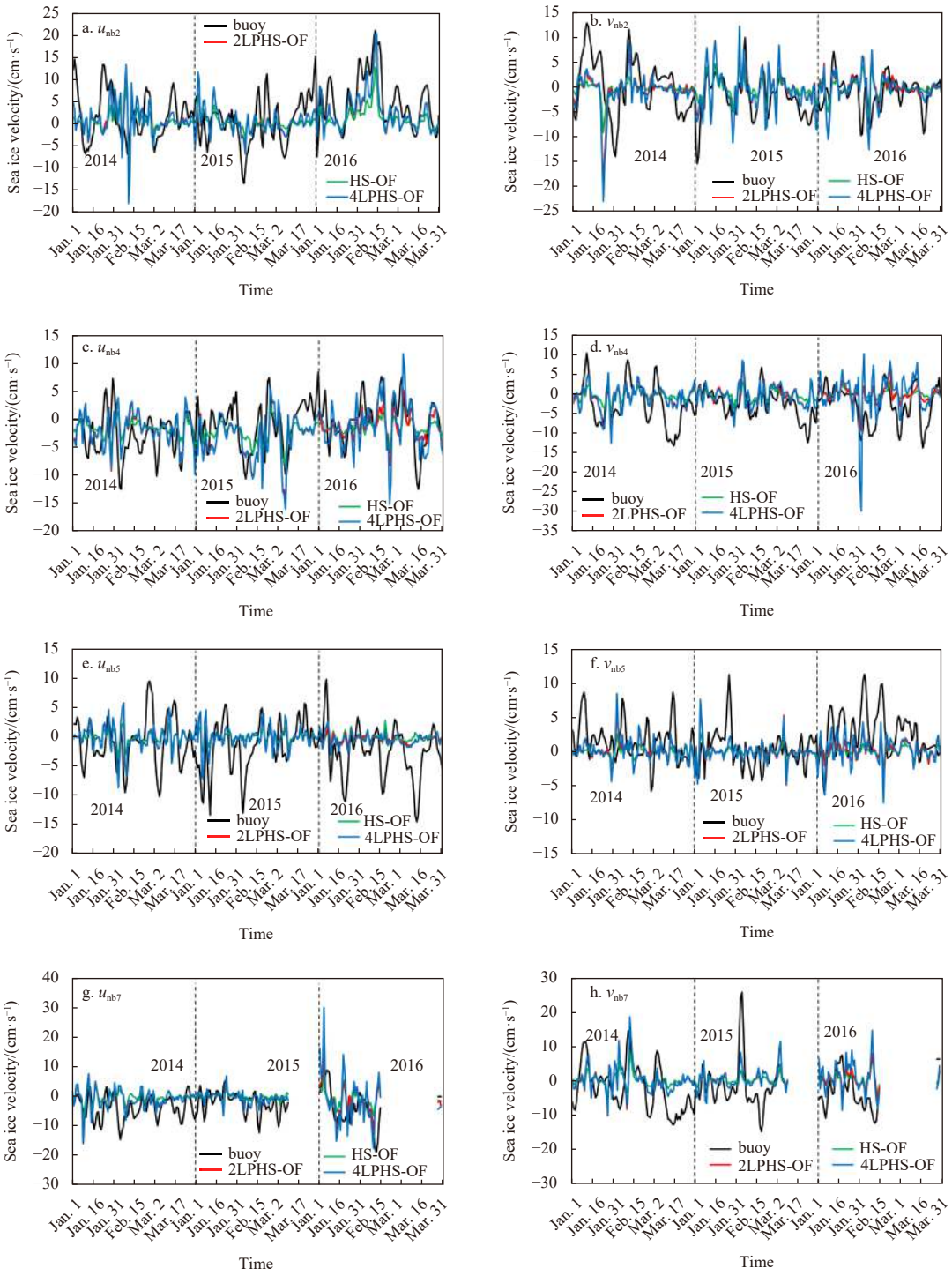

Fig. 5. The daily sea ice velocity in winter from 2014 to 2016 in the *u*-direction and *v*-direction, which are obtained from buoys and by the HS-OF, 2LPHS-OF and 4LPHS-OF methods. a, c, e and g. Velocities at the nb2, nb4, nb5 and nb7 positions in the *u*-direction; and b, d, f and h. velocity at the nb2, nb4, nb5 and nb7 positions in the *v*-direction.

creases the overestimation, and the use of four pyramid layers further enlarges the error. It produces errors in image reconstruction. With an increase in the number of layers and a decrease in the size of the image, the error in image reconstruction increases. If the velocity is overestimated in the top layer, then the speed will be further overestimated by layer iteration. The variation in sea ice velocity obtained by pyramid stratification is more consistent with that of the buoy. The consistency of the *u*-velocity is better than that of the *v*-velocity. Compared with the HS-OF velocity (without pyramid stratification), the 2LPHS-OF velocity is much higher, and the 4LPHS-OF velocity is slightly higher than the 2LPHS-OF velocity. Sea ice velocities are more accurate in the East Siberian Sea and Laptev Sea than in the Canadian Archipelago, Kara and Barents seas (Fig. 5). The velocities in the Canadian Archipelago, Kara and Barents seas are underestimated, especially in the *u*-direction (Figs 5e and g).

Although the 4LPHS-OF velocity is larger than the 2LPHS-OF velocity, there is an overestimation of the sea ice speed, resulting in a larger error (Table 3). In addition, due to the increase in the number of pyramid layers, the corresponding computation cost also increases. This study indicates that the 2-layer pyramid is more suitable for the estimation of winter Arctic ice drift; thus, the sea ice velocity obtained by the 2LPHS-OF method is selected for discussion and analysis in the following chapters.

3.2 *The 2LPHS-OF velocity and drift products comparations*

To prove the advantages of the 2LPHS-OF method for estimating velocity, we analyze the accuracy of the OSI SAF and CMEMS datasets. Comparing the results shown in Tables 3 and 4, we find that the 2LPHS-OF velocity has a lower RMSE and MAE with a higher correlation than the OSI SAF data, especially in the v-direction (RMSE: decreases 33%; ME: decreases 56%; MAE: decreases 26%; P: improves 41%). The 2LPHS-OF velocity has a lower RMSE (u-direction: 25%; v-direction: 16%) and MAE (u-direction: 27%; v-direction: 16%) but a higher ME and a lower correlation than the CMEMS data.

We select the same positions (i.e., nb2, nb4, nb5 and nb7) to analyze variations in the sea ice motion datasets from 2014 to 2016 as well as the buoy velocity. Generally, the speeds from the two datasets are higher than the buoy velocity (Fig. 6). The OSI SAF dataset greatly overestimates the ice velocity, especially in 2014 and 2015. At some times, it yields velocity in the opposite direction, such as the velocity at the nb4 position in March (Fig. 6c). The CMEMS dataset is more consistent with respect to buoy velocity than the OSI SAF dataset and 2LPHS-OF velocity in 2014 and 2015 (Figs 5 and 6), but it is less consistent with buoy velocity in 2016, especially in the Canadian Archipelago and the Kara and Barents seas (Figs 6f and h).

The NSIDC dataset merges the buoy velocity, and it has a higher RMSE in the u-direction (4.82 cm/s), a lower RMSE in the v-direction (3.92 cm/s) and higher P in both the u- and v-directions than the 2LPHS-OF velocity. Then, we take the NSIDC velocity as a basis and evaluate the consistency between the 2LPHS-OF velocity and NSIDC velocity. The Pearson correlation coefficient between the average 2LPHS-OF velocity and average NSIDC product in the Arctic is obtained as well as the RMSE, ME, MAE and P. The results show that the 2LPHS-OF velocity has a significant positive correlation with the NSIDC velocity at the 0.01 significance level (u-direction: 0.40; v-direction: 0.62). The RMSE, ME and MAE are less than 2 cm/s in both the u- and v-directions, and P is higher than 0.60, indicating good consistency between these two velocities (Table 5). Therefore, the sea ice drift algorithm developed in this study can effectively estimate the sea ice velocity and matches well-known international datasets. Furthermore, in some regions, it offers more accurate vectors.

3.3 *Error analysis of 2LPHS-OF velocity*

The error of the 2LPHS-OF velocity is affected by three factors. First, the accuracy of the estimated results is restricted by the accuracy of the remote sensing equipment (Li et al., 2019). There are ineluctable errors in the measurement, acquisition and calculation of satellite data. Second, any model, even well-developed methods (Rostosky et al., 2018), cannot simulate physical parameters accurately; a model can only provide results that are as close as possible to the actual value. Although the 2LPHS-OF method produces errors in pyramid image construction, it largely satisfies the constraint condition of small motion and ultimately reduces the sea ice velocity estimation error. Third, factors such as snowfall and sea ice melting affect the error of the 2LPHS-OF velocity. Optical flow methods are based on the brightness constancy assumption (Petrou and Tian, 2017). When there is larger snowfall or dramatic sea ice melting, the brightness temperature of a pixel changes as it moves, causing errors in estimated sea ice velocity. The estimated velocity in the Atlantic sector of the Arctic (the Canadian Archipelago, the Kara and Barents seas) is less accurate than that in the Pacific sector of the Arctic (the East Siberian Sea, the Laptev Sea) (Table 5), which may result from larger snowfall and snow accumulation in the Atlantic sector of the Arctic (Petty et al., 2018).

4 The variation in winter Arctic sea ice velocity in 2016

4.1 *Spatial distribution of the sea ice velocity*

The spatial distribution of the ice velocity between January and March is obtained by selecting the sea ice velocity on the 1st and 15th of each month (Fig. 7). The results show that the sea ice coverage increases with time. From January 1 to January 15, the maximum sea ice velocity in the Kara Sea moves to the FS. The sea ice velocity reaches the maximum in the FS on January 15. Then, it decreases slightly and then increases, reaching a maximum again on March 1. In January, the ice velocity in the Bering Sea is generally low; on February 1, the velocity in this area increases significantly, and it greatly increases in the Bering Strait. On February 15, the increasing area in the Bering Strait further expands and then begins to decrease. On March 15, the sea ice velocity in the whole study area is generally low, except in the Kara Sea (Fig. 7).

On January 1, the sea ice flows into the Kara Sea; afterwards, the sea ice is transported from the Kara Sea to the outside of the Kara Sea until March (Fig. 7). On January 1, some sea ice in the FS is imported into the Arctic Ocean and some is exported from the Arctic Ocean, while on January 15, February 1, March 1 and 15, it is mainly exported from the Arctic Ocean. This reveals that FS is a major export channel for sea ice loss in winter. In January, the sea ice in the Bering Strait is mainly exported from the Arctic Ocean to the Bering Sea; from February to March, the sea ice in the Bering Strait is mainly exported from the Bering Sea to the Arctic Ocean, which is opposite to the direction of sea ice flow in January. There are two main characteristics of Arctic sea ice mo-

Table 4. Accuracy evaluation of the OSI SAF and CMEMS vectors in the u- and v-directions through the RMSE, ME, MAE, and P values based on buoy velocity

	u		v	
	OSI SAF	CMEMS	OSI SAF	CMEMS
RMSE/(cm·s^{-1})	6.28 (24%)	6.36 (25%)	6.98 (33%)	5.60 (16%)
ME/(cm·s^{-1})	0.57 (60%)	0.15 (–56%)	1.22 (56%)	0.35 (–55%)
MAE/(cm·s^{-1})	4.50 (20%)	4.93 (27%)	4.73 (26%)	4.16 (16%)
P	0.64 (8%)	0.87 (–25%)	0.43 (41%)	0.78 (–29%)

Note: The values in brackets indicate the percentage improvement of the accuracy indices of the 2LPHS-OF velocity relative to the accuracy indices of the other data.

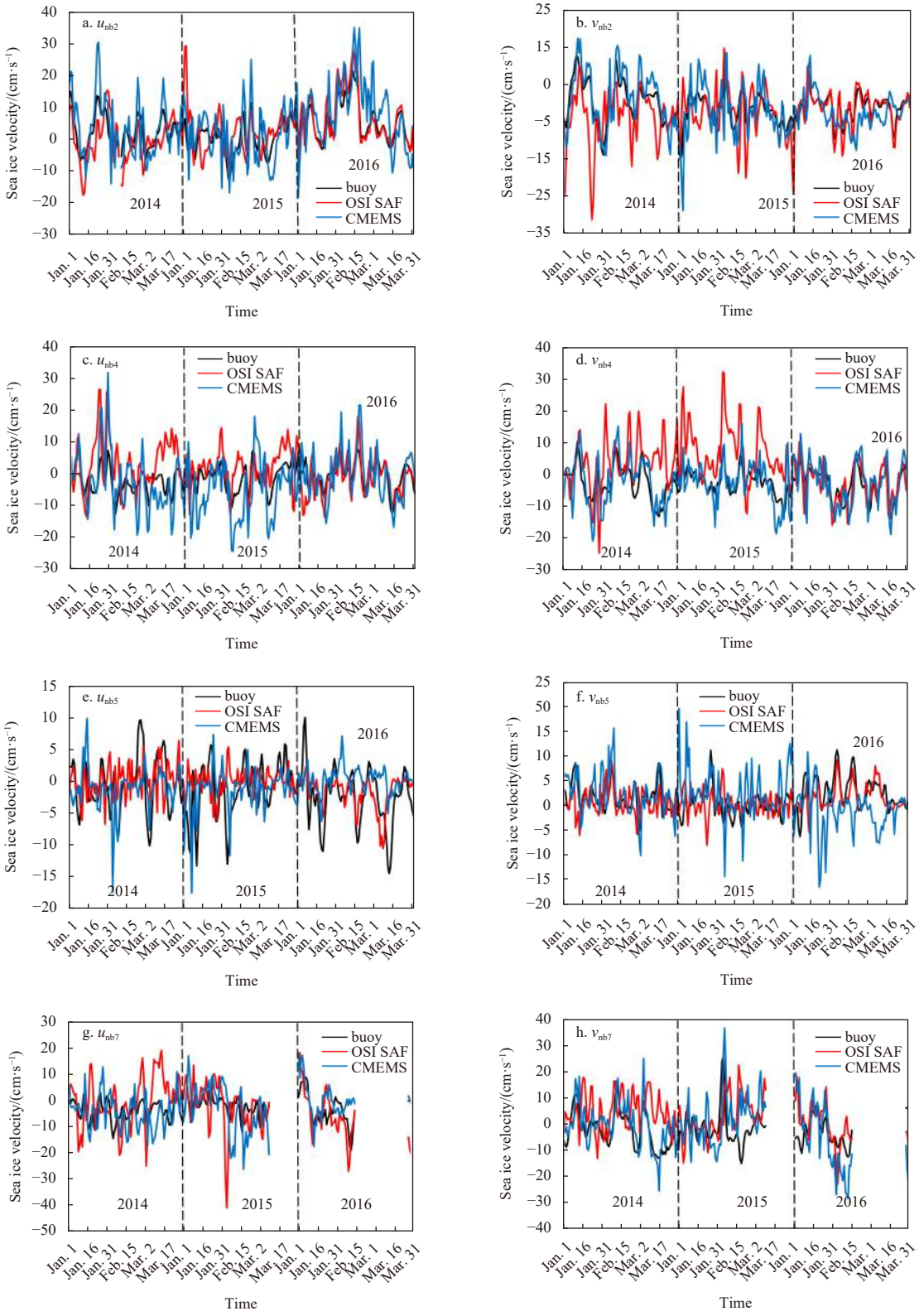

Fig. 6. The daily sea ice velocity in winter from 2014 to 2016 in the *u*-direction and *v*-direction, which are obtained from buoys and the OSI SAF and CMEMS dataset. a, c, e and g. Velocities at the nb2, nb4, nb5 and nb7 positions in the *u*-direction; and b, d, f and h. velocities at the nb2, nb4, nb5 and nb7 positions in the *v*-direction.

tion in winter: transpolar drift (TPD) and the Beaufort Gyre (BG). This finding is consistent with the analytical results obtained by Tian et al. (2012). As shown in Fig. 7, the blue box indicates the occurrence of the Arctic cyclone, and the black box indicates the occurrence of the Arctic anticyclone (including the BG). On January 1, the Arctic sea ice moves from the ESS to the Canadian Ar-

Table 5. Evaluation of the 2LPHS-OF vectors in the u- and v-directions through the RMSE, ME, MAE, and P based on NSIDC velocity data from 2014 to 2016

	RMSE/(cm·s^{-1})	ME/(cm·s^{-1})	MAE/(cm·s^{-1})	P
u	1.90	0.90	1.45	0.62
v	1.99	0.91	1.64	0.80

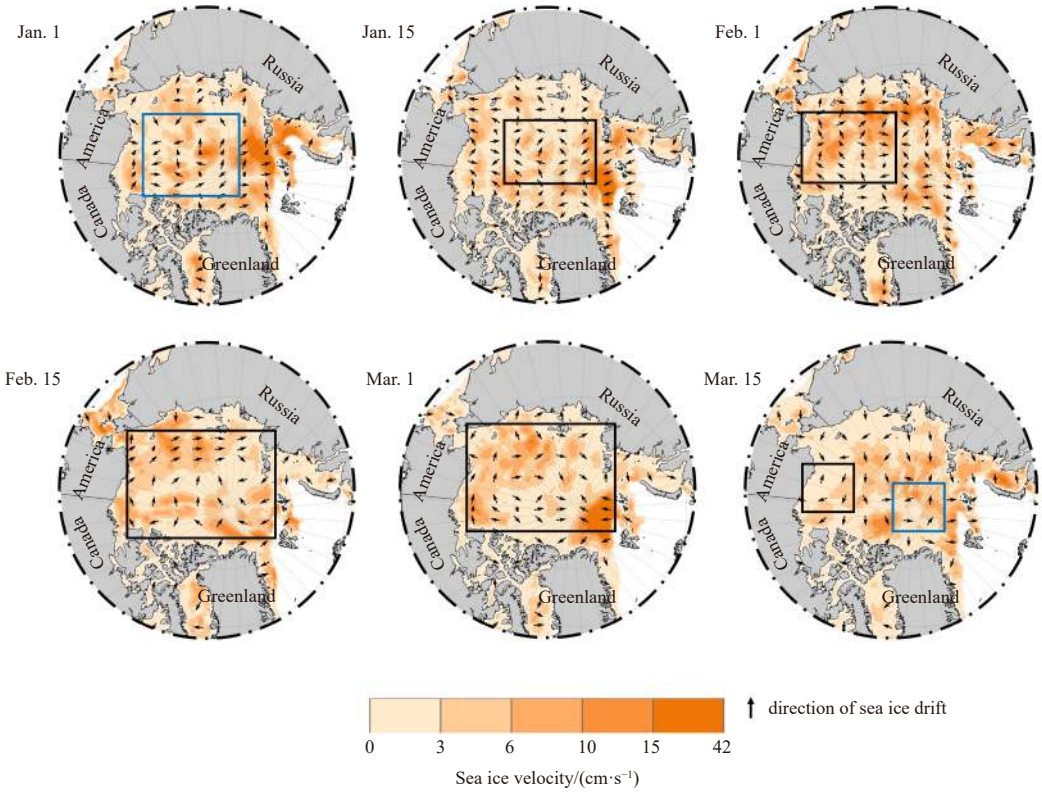

Fig. 7. Spatial distribution of the sea ice drift velocity on the 1st and 15th days of each month in the Arctic in 2016. The blue box indicates the occurrence of the Arctic cyclone, and the black box indicates the occurrence of the Arctic anticyclone, including the Beaufort Gyre.

chipelago. At the same time, the Arctic sea ice also shows cyclonic motion. On January 15, there is anticyclonic movement in the Arctic Ocean, and on February 1, the BG (anticyclonic movement) appears in northern America, and the BG is more obvious and wider on February 15 and March 1. On March 15, the BG is small and at the same time, there is an Arctic cyclone near the pole. On February 1, the sea ice moves from the LS to the FS and the Greenland Sea. On March 15, the sea ice shows TPD, moving from the ESS and the LS to the Greenland Sea and the FS.

4.2 *Variations in sea ice velocity in nine subregions*

The average winter sea ice velocity in the Kara and Barents seas is the highest at (2.07 ± 1.10) cm/s and that of the Canadian Archipelago is the lowest at (0.14 ± 0.08) cm/s in 2016 (Table 6). From January to March 2016, the sea ice velocity in the Bering Sea, the seas of Okhotsk and Japan, and the Gulf of St. Lawrence increases month by month at rates of 0.005 cm/(s·d) (d is day), 0.025 cm/(s·d) (significant at the 0.01 level) and 0.015 cm/(s·d), respectively (Table 6 and Fig. 8). The sea ice velocity in the Kara and Barents seas decreases month by month at a rate of –0.006 cm/(s·d). The sea ice velocity in the remaining five subregions first decreases and then increases (Fig. 8).

The increase in the sea ice velocity in the Hudson Bay, the Gulf of St. Lawrence, the Bering Sea, and the seas of Okhotsk and Japan may be related to sea ice retreat time and the length of the open water season. All of those regions are located at lower latitudes than other regions, and the Gulf of St. Lawrence has the longest open water season, which is approximately 300 d (Li and Ke, 2017). In addition, sea ice in the Bering Sea and the seas of Okhotsk and Japan retreats early, and the length of the open water season is more than 200 d (Li and Ke, 2017). We further dis-

Table 6. Statistics for sea ice velocity in nine subregions of the Arctic

Region	Mean /(cm·s^{-1})	SD /(cm·s^{-1})	Speed rate /(cm·s^{-1}·d^{-1})
Arctic Ocean	1.39	0.70	–0.003 0
Canadian Archipelago	0.14	0.08	–0.000 2
Bering Sea	1.20	1.26	**0.005 0**
Seas of Okhotsk and Japan	1.91	1.26	**0.025 0**[1)]
Kara and Barents seas	2.07	1.10	–0.006 0
Greenland Sea	1.15	0.74	–0.003 0
Hudson Bay	0.77	0.92	**0.009 0**[2)]
Baffin Bay/Labrador Sea	1.20	0.56	–0.001 0
Gulf of St. Lawrence	0.62	1.00	**0.015 0**

Note: [1)] Probability value < 0.01. [2)] Probability value < 0.05. Bolded values indicate a speed rate greater than 0.

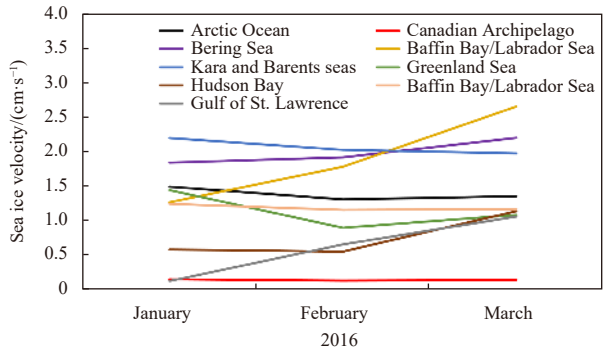

Fig. 8. The monthly sea ice velocity in nine subregions from January to March, 2016.

cuss the relationship between sea ice velocity and open water area (OWA). The velocities in the Arctic Ocean and the Kara and Barents Seas have significant positive correlations with the OWA, while those in the Gulf of St. Lawrence and the seas of Okhotsk and Japan have significant negative correlations with the OWA. The latter two regions have an early sea ice retreat time, and as the OWA decreases, the sea ice velocity can still increase. Generally, when the OWA decreases, velocities decrease, but when the sea ice retreats early with a longer open water season, the sea ice velocity increases in winter.

5 Conclusions

We improve the HS-OF method by combining it with a pyramid algorithm. The winter sea ice velocities derived from the HS-OF, 2LPHS-OF and 4LPHS-OF methods are compared with the buoy-interpolated velocity. We further compare the 2LPHS-OF velocity with other commonly used sea ice motion datasets. We draw the following conclusions:

(1) The proposed PHS-OF method is more accurate than the HS-OF method for sea ice velocity estimation, especially in the u-direction. This greatly improves the correlation between the obtained velocity and the buoy velocity. Compared with the 4LPHS-OF method, the 2LPHS-OF method is more suitable for winter sea ice velocity estimation because it has a higher accuracy and shorter computing time.

(2) The 2LPHS-OF velocity is an underestimation of the ice velocity, while commonly used sea ice drift products including the LR OSI SAF product and CMEMS product are overestimations of the sea ice velocity. The 2LPHS-OF velocity has a smaller error than the LR OSI SAF product and CMEMS product. The 2LPHS-OF velocity has a smaller RMSE than the NSIDC velocity in the u-direction, while it has a larger RMSE than the NSIDC velocity in the v-direction. In addition, variations in sea ice velocity are consistent with those of the NSIDC motion dataset in the Arctic, and the bias between these two datasets is less than 1 cm/s in both the u- and v-directions. Therefore, the velocity obtained by the 2LPHS-OF method can be used to analyze the variation in sea ice velocity.

(3) The obtained results show that the winter sea ice in 2016 is mainly in the form of TPD and BG, and there are also cyclonic motions and anticyclonic motions of sea ice in the Arctic Ocean. The change in the winter sea ice velocity is related to the OWA, sea ice retreat time and length of the open water season. When the sea ice retreat time is early with a longer open water season, the sea ice velocity shows an increasing trend.

(4) Although the 2LPHS-OF method is more accurate than the HS-OF method, it still underestimates the winter sea ice velocity, especially in regions where sea ice moves fast. How to further solve the underestimation tendency of the 2LPHS-OF method is the next focus of our research. Furthermore, we will use multiple sensors to obtain the sea ice velocity, carry out the merging operation, and then merge the buoy data with the sea ice velocity data in the future.

Acknowledgements

We thank the National Snow and Ice Data Center for the brightness temperature, sea ice concentration and sea ice motion data, the International Arctic Buoy Programme for the buoy data, the Ocean and Sea Ice Satellite Application Facility for the low-resolution sea ice drift data, and the Copernicus Marine Environment Monitoring Service for the sea ice motion data.

References

Agnew T A, Le Hao, Hirose T. 1997. Estimation of large-scale sea-ice motion from SSM/I 85.5 GHz imagery. Annals of Glaciology, 25: 305–311, doi: 10.3189/S0260305500014191

Allison I. 1989. Pack-ice drift off East Antarctica and some implications. Annals of Glaciology, 12: 1–8, doi: 10.3189/S0260305500006881

Arrigo K R, Van Dijken G L. 2011. Secular trends in Arctic Ocean net primary production. Journal of Geophysical Research: Oceans, 116(C9): C09011

Berg A, Eriksson L E B. 2014. Investigation of a hybrid algorithm for sea ice drift measurements using synthetic aperture radar images. IEEE Transactions on Geoscience and Remote Sensing, 52(8): 5023–5033, doi: 10.1109/TGRS.2013.2286500

Borcea L, Callaghan T, Papanicolaou G. 2012. Synthetic aperture radar imaging and motion estimation via robust principal component analysis. SIAM Journal on Imaging Sciences, 6(3): 1445–1476

Cavalieri D J, Parkinson C L, Vinnikov K Y. 2003. 30-year satellite record reveals contrasting Arctic and Antarctic decadal sea ice variability. Geophysical Research Letters, 30(18): 1970

Choudhary B K, Sinha N K, Shanker P. 2012. Pyramid method in image processing. Journal of Information Systems and Communication, 3(1): 269–273

Copernicus Marine Service (CMEMS). 2020. Product user manual for Arctic Ocean physical and BGC analysis and forecasting products. Issue 5.12. http://marine.copernicus.eu/documents/PUM/CMEMS-ARC-PUM-002-ALL.pdf [2020-04/2021-01-10]

Comiso J C, Meier W N, Gersten R. 2017. Variability and trends in the arctic sea ice cover: results from different techniques. Journal of Geophysical Research:Oceans, 122(8): 6883–6900, doi: 10.1002/2017JC012768

Deng Juan. 2014. Northern Hemisphere sea ice variability and its relationship with climate factors (in Chinese) [dissertation]. Nanjing: Nanjing University

Emery W J, Fowler C W, Maslanik J A. 1997. Satellite-derived maps of Arctic and Antarctic sea ice motion: 1988 to 1994. Geophysical Research Letters, 24(8): 897–900, doi: 10.1029/97GL00755

Fleet D, Weiss Y. 2006. Optical flow estimation. In: Paragios N, Chen Yunmei, Faugeras O, eds. Handbook of Mathematical Models in Computer Vision. Boston: Springer, 237–257

Girard-Ardhuin F, Ezraty R. 2012. Enhanced arctic sea ice drift estimation merging radiometer and scatterometer data. IEEE Transactions on Geoscience and Remote Sensing, 50(7): 2639–2648, doi: 10.1109/TGRS.2012.2184124

Gutiérrez S, Long D G. 2003. Optical flow and scale-space theory applied to sea-ice motion estimation in Antarctica. In: Proceedings of 2003 IEEE International Geoscience and Remote Sensing Symposium. Toulouse: IEEE, 2805–2807

Horn B K P, Schunck B G. 1981. Determining optical flow. Artificial Intelligence, 17(1–3): 185–203, doi: 10.1016/0004-3702(81)90024-2

Ke Ruimin, Li Zhibin, Tang Jinjun, et al. 2019. Real-time traffic flow

parameter estimation from UAV video based on ensemble classifier and optical flow. IEEE Transactions on Intelligent Transportation Systems, 20(1): 54–64, doi: 10.1109/TITS.2018.2797697

Ke Changqing, Peng Haitao, Sun Bo, et al. 2013. Spatio-temporal variability of Arctic sea ice from 2002 to 2011. Journal of Remote Sensing (in Chinese), 17(2): 452–466

Komarov A S, Barber D G. 2014. Sea ice motion tracking from sequential dual-polarization Radarsat-2 Images. IEEE Transactions on Geoscience and Remote Sensing, 52(1): 121–136, doi: 10.1109/TGRS.2012.2236845

Kwok R, Schweiger A, Rothrock D A, et al. 1998. Sea ice motion from satellite passive microwave imagery assessed with ERS SAR and buoy motions. Journal of Geophysical Research:Oceans, 103(C4): 8191–8214, doi: 10.1029/97JC03334

Kwok R, Spreen G, Pang S. 2013. Arctic sea ice circulation and drift speed: decadal trends and ocean currents. Journal of Geophysical Research: Oceans, 118(5): 2408–2425, doi: 10.1002/jgrc.20191

Lan Jinhui, Li Jian, Hu Guangda, et al. 2014. Vehicle speed measurement based on gray constraint optical flow algorithm. Optik, 125(1): 289–295, doi: 10.1016/j.ijleo.2013.06.036

Lavergne T, Eastwood S, Teffah Z, et al. 2010. Sea ice motion from low-resolution satellite sensors: an alternative method and its validation in the arctic. Journal of Geophysical Research: Oceans, 115(C10): C10032

Lehtiranta J, Siiriä S, Karvonen J. 2015. Comparing C- and L-Band SAR images for sea ice motion estimation. The Cryosphere, 9(1): 357–366, doi: 10.5194/tc-9-357-2015

Li Haili, Ke Changqing. 2017. Open water variability in the North Pole from 1982 to 2016. Haiyang Xuebao (in Chinese), 39(12): 109–121

Li Haili, Ke Changqing, Zhu Qinghui, et al. 2019. Spatial-temporal variations in net primary productivity in the Arctic from 2003 to 2016. Acta Oceanologica Sinica, 38(8): 111–121, doi: 10.1007/s13131-018-1274-5

Lim A, Ramesh B, Yang Yue, et al. 2019. Real-time optical flow-based video stabilization for unmanned aerial vehicles. Journal of Real-Time Image Processing, 16(6): 1975–1985, doi: 10.1007/s11554-017-0699-y

Liu A K, Cavalieri D J. 1998. On sea ice drift from the wavelet analysis of the defense meteorological satellite program (DMSP) special sensor microwave imager (SSM/I) data. International Journal of Remote Sensing, 19(7): 1415–1423, doi: 10.1080/014311698215522

Liu Yige, Ke Changqing, Zhang Jie. 2019. Analysis of kinematic characteristics of Antarctic sea ice from 1979 to 2014. Chinese High Technology Letters (in Chinese), 29(1): 90–98

Liu A K, Zhao Yunhe, Wu S Y. 1999. Arctic sea ice drift from wavelet analysis of NSCAT and special sensor microwave imager data. Journal of Geophysical Research: Oceans, 104(C5): 11529–11538, doi: 10.1029/1998JC900115

Mäkynen M, Haapala J, Aulicino G, et al. 2020. Satellite observations for detecting and forecasting sea-ice conditions: a summary of advances made in the SPICES project by the EU's Horizon 2020 Programme. Remote Sensing, 12(7): 1214, doi: 10.3390/rs12071214

Massom R A, Stammerjohn S E. 2010. Antarctic sea ice change and variability—physical and ecological implications. Polar Science, 4(2): 149–186, doi: 10.1016/j.polar.2010.05.001

Meier W N, Dai Mingrui. 2006. High-resolution sea-ice motions from AMSR-E imagery. Annals of Glaciology, 44: 352–356, doi: 10.3189/172756406781811286

Min Chao, Mu Longjiang, Yang Qinghua, et al. 2019. Sea ice export through the Fram Strait derived from a combined model and satellite data set. The Cryosphere, 13(12): 3209–3224, doi: 10.5194/tc-13-3209-2019

Muckenhuber S, Korosov A A, Sandven S. 2016. Open-source feature-tracking algorithm for sea ice drift retrieval from sentinel-1 SAR imagery. The Cryosphere, 10(2): 913–925, doi: 10.5194/tc-10-913-2016

Muckenhuber S, Sandven S. 2018. Sea ice drift data for Fram Strait derived from a feature-tracking algorithm applied on sentinel-1 SAR imagery. Data in Brief, 18(2018): 1410–1415, doi: 10.1016/j.dib.2018.04.034

Ninnis R M, Emery W J, Collins M J. 1986. Automated extraction of pack ice motion from advanced very high resolution radiometer imagery. Journal of Geophysical Research:Oceans, 91(C9): 10725–10734, doi: 10.1029/JC091iC09p10725

NSIDC. 2019. Polar pathfinder daily 25 km EASE-grid sea ice motion vectors, version 4-user guide. https://nsidc.org/data/NSIDC-0116/versions/4 [2019-02-25/2020-01-08]

Cavalieri D J, Parkinson C L. 2012. Arctic sea ice variability and trends, 1979–2010. The Cryosphere, 6(4): 881–889

Parkinson C L, Cavalieri D J, Gloersen P, et al. 1999. Arctic sea ice extents, areas, and trends, 1978–1996. Journal of Geophysical Research: Oceans, 104(C9): 20837–20856, doi: 10.1029/1999JC900082

Peng Ge, Meier W N. 2018. Temporal and regional variability of arctic sea-ice coverage from satellite data. Annals of Glaciology, 59(76pt2): 191–200, doi: 10.1017/aog.2017.32

Petrou Z I, Tian Yingli. 2017. High-resolution sea ice motion estimation with optical flow using satellite spectroradiometer data. IEEE Transactions on Geoscience and Remote Sensing, 55(3): 1339–1350, doi: 10.1109/TGRS.2016.2622714

Petrou Z I, Xian Yang, Tian Yingli. 2018. Towards breaking the spatial resolution barriers: an optical flow and super-resolution approach for sea ice motion estimation. ISPRS Journal of Photogrammetry and Remote Sensing, 138: 164–175, doi: 10.1016/j.isprsjprs.2018.01.020

Petty A A, Webster M, Boisvert L, et al. 2018. The NASA Eulerian snow on sea ice model (NESOSIM) v1.0: initial model development and analysis. Geoscientific Model Development, 11(11): 4577–4602, doi: 10.5194/gmd-11-4577-2018

Qiu Bowei, Li Chunhua, Guan Changlong, et al. 2019. The influence of sea ice drift on the distribution of multiyear ice. Transactions of Oceanology and Limnology (in Chinese), (3): 1–11

Rossel R A V, Webster R. 2012. Predicting soil properties from the australian soil visible-near infrared spectroscopic database. European Journal of Soil Science, 63(6): 848–860, doi: 10.1111/j.1365-2389.2012.01495.x

Rostosky P, Spreen G, Farrell S L, et al. 2018. Snow depth retrieval on Arctic sea ice from passive microwave radiometers—improvements and extensions to multiyear ice using lower frequencies. Journal of Geophysical Research: Oceans, 123(10): 7120–7138, doi: 10.1029/2018JC014028

Sakov P, Counillon F, Bertino L, et al. 2012. TOPAZ4: an ocean-sea ice data assimilation system for the North Atlantic and Arctic. Ocean Science, 8(4): 633–656, doi: 10.5194/os-8-633-2012

Tian Zhongxiang, Li Chunhua, Zhang Lin, et al. 2012. Climatology characteristics of Arctic sea ice motion. Marine Forecasts (in Chinese), 29(6): 66–73

Wang Liya, He Yijun, Zhang Biao, et al. 2017. Retrieval of Arctic sea ice drift using HY-2 satellite scanning microwave radiometer data. Haiyang Xuebao (in Chinese), 39(9): 110–120

Wu Qing, Lang Wenhui, Zhang Xi, et al. 2014. Sea ice drift tracking in the Bohai Sea based on optical flow. In: Proceedings of SPIE 9159 Sixth International Conference on Digital Image Processing (ICDIP 2014). Athens: SPIE

Zhang Jinlun, Rothrock D, Steele M. 2000. Recent changes in Arctic sea ice: the interplay between ice dynamics and thermodynamics. Journal of Climate, 13(17): 3099–3114, doi: 10.1175/1520-0442(2000)013<3099:RCIASI>2.0.CO;2

Zhao Yunhe, Liu A K. 2007. Arctic sea-ice motion and its relation to pressure field. Journal of Oceanography, 63(3): 505–515, doi: 10.1007/s10872-007-0045-2

Zhu Wenbin, Jia Shaofeng, Lv Aifeng. 2014. Monitoring the fluctuation of Lake Qinghai using multi-source remote sensing data. Remote Sensing, 6(11): 10457–10482, doi: 10.3390/rs61110457

Zuo Zhengdao, Gao Guoping, Cheng Lingqiao, et al. 2016. Preliminary analysis of kinematic characteristics of Arctic sea ice from 1979 to 2012. Haiyang Xuebao (in Chinese), 38(5): 57–69